





Article

High Resolution Powder Electron Diffraction in Scanning Electron Microscopy

Miroslav Slouf ^{1,*} , Radim Skoupy ² , Ewa Pavlova ¹  and Vladislav Krzyzanek ^{2,*} 

¹ Institute of Macromolecular Chemistry of the Czech Academy of Sciences, Heyrovsky Sq. 2, 16206 Prague, Czech Republic; pavlova@imc.cas.cz

² Institute of Scientific Instruments of the Czech Academy of Sciences, Kralovopolska 147, 61264 Brno, Czech Republic; radim.skoupy@isibrno.cz

* Correspondence: slouf@imc.cas.cz (M.S.); krzyzanek@isibrno.cz (V.K.)

Abstract: A modern scanning electron microscope equipped with a pixelated detector of transmitted electrons can record a four-dimensional (4D) dataset containing a two-dimensional (2D) array of 2D nanobeam electron diffraction patterns; this is known as a four-dimensional scanning transmission electron microscopy (4D-STEM). In this work, we introduce a new version of our method called 4D-STEM/PNBD (powder nanobeam diffraction), which yields high-resolution powder diffractograms, whose quality is fully comparable to standard TEM/SAED (selected-area electron diffraction) patterns. Our method converts a complex 4D-STEM dataset measured on a nanocrystalline material to a single 2D powder electron diffractogram, which is easy to process with standard software. The original version of 4D-STEM/PNBD method, which suffered from low resolution, was improved in three important areas: (i) an optimized data collection protocol enables the experimental determination of the point spread function (PSF) of the primary electron beam, (ii) an improved data processing combines an entropy-based filtering of the whole dataset with a PSF-deconvolution of the individual 2D diffractograms and (iii) completely re-written software automates all calculations and requires just a minimal user input. The new method was applied to Au, TbF₃ and TiO₂ nanocrystals and the resolution of the 4D-STEM/PNBD diffractograms was even slightly better than that of TEM/SAED.

Keywords: nanoparticle analysis; powder nanobeam electron diffraction; 4D-STEM



Citation: Slouf, M.; Skoupy, R.; Pavlova, E.; Krzyzanek, V. High Resolution Powder Electron Diffraction in Scanning Electron Microscopy. *Materials* **2021**, *14*, 7550. <https://doi.org/10.3390/ma14247550>

Academic Editor: Nabila Maloufi

Received: 18 November 2021

Accepted: 7 December 2021

Published: 9 December 2021

Publisher's Note: MDPI stays neutral with regard to jurisdictional claims in published maps and institutional affiliations.



Copyright: © 2021 by the authors. Licensee MDPI, Basel, Switzerland. This article is an open access article distributed under the terms and conditions of the Creative Commons Attribution (CC BY) license (<https://creativecommons.org/licenses/by/4.0/>).

1. Introduction

Scanning electron microscopy (SEM) is a well-established method for characterization of materials in both micro- and nanoscale. The classical modes of SEM comprise imaging with secondary electrons (SE), backscattered electrons (BSE) and transmitted electrons (scanning transmission electron microscopy; STEM), and microanalysis (energy-dispersive analysis of X-rays; EDX). In the field of STEM, the standard detectors collect just the integral signal from the electrons going through the specimen almost directly (bright field imaging, BF) or from the electrons scattered at higher angles (annular dark field imaging, ADF, and high-angle annular dark field imaging, HAADF).

The standard STEM/BF, STEM/ADF and STEM/HAADF micrographs are two-dimensional (2D-STEM), i.e., every XY-position on the sample gives one signal on the detector [1]. However, the fact that STEM imaging might yield more information, on the condition that it was possible to record positions of the scattered electrons, did not escape the attention of researchers. An intermediate step was the commercialization of multi-segmental STEM detectors, which consisted of one central segment in BF region and multiple annular (or semi-annular) segments in ADF and HAADF regions [2,3]. For each XY-position on the sample, the multi-segmental STEM detector can yield signal from each of its segments. This is occasionally called **multidimensional STEM**, where the additional dimension is the angular resolution [4]. The final step was the recent commercialization of 2D-array detectors (also known as pixelated detectors). The pixelated STEM detectors

record both the intensity and position of the scattered electrons, i.e., they record a 2D diffraction pattern for each beam position. If the scanning beam is narrow and non-convergent, the recorded pattern corresponds to nanobeam diffraction (NBD) known from TEM (but the classical TEM/NBD measurements are performed with a fixed, non-scanning beam [5]). As the diffraction patterns are recorded for all XY-positions of the primary beam on the specimen, we get a 4D data cube (a 2D array of 2D diffraction patterns) and the technique is referred to as **4D-STEM**. The traditional pixelated STEM detectors are indirect, combining a scintillator (a material converting ionizing radiation to light) with a digital camera based on CCD (charge coupled device) or CMOS (complementary metal oxide semiconductor) technology; these devices suffer from somewhat lower speed and/or higher noise. The modern pixelated STEM detectors are direct (DED; direct electron detectors) and exhibit higher speed, lower noise, and smaller size in comparison with traditional CCD and CMOS cameras [6,7].

The 4D-STEM techniques were introduced in the field of TEM and dedicated high-energy STEM microscopes, where they have already found numerous applications as summarized in recent reviews [8,9]. In the field of SEM, the 4D-STEM techniques are much less common. The fast pixelated DED detectors for SEM were commercialized quite recently [10]. Consequently, just a few examples of 4D-STEM in SEM can be found in the literature, and most of the studies were based on traditional CCD and CMOS detectors [11–14]. This resulted in somewhat non-standard hardware solutions, in which bulky CCD and CMOS cameras had to be attached to adjusted SEM columns. Moreover, the authors focused their attention on the analysis of the individual diffraction patterns of the 4D dataset, which required detailed crystallographic knowledge and special software. In contrast, our recent study [15] was focused on simple, fast, and efficient usage of 4D-STEM method in everyday life. In our method, which was called 4D-STEM/PNBD (powder nanobeam diffraction), we combine all diffraction patterns (showing diffraction spots from one or more nanocrystals) into a single powder diffraction pattern (showing diffraction rings typical of polycrystalline samples). In this way, we converted the complex 4D dataset into a simple 2D powder diffractogram. We analyzed several sets of inorganic nanocrystals deposited on thin carbon film and the 4D-STEM/PNBD diffraction patterns corresponded to the well-known TEM/SAED (selected-area electron diffraction) patterns. Consequently, the 4D-STEM/PNBD and TEM/SAED diffractograms could be processed with the same, well-established programs, such as *ProcessDiffraction* [16]. These programs do not require deep crystallographic knowledge, as the processing of powder diffractograms is quite straightforward. The measurements were performed with a high-resolution SEM microscope equipped with a fast DED detector. The small DED detector can be mounted in any modern SEM microscope with a standard port for STEM, which makes the method accessible to all users of modern SEM's.

In this contribution, we have resolved the most important limitation of the previous version of our 4D-STEM/PNBD method, which consisted of the lower-intensity, broader diffraction peaks in comparison with TEM/SAED. The current version 4D-STEM/PNBD method has been improved in three important aspects: At first, we optimized the measurement protocol so that we could get the accurate point spread function (PSF) of the primary beam. At second, we combined entropy-based filtering of the whole 4D dataset with PSF-deconvolution of the individual 2D diffractograms, which lead to a significant enhancement of both intensities and resolution of the diffraction peaks. At third, we upgraded our Python package *STEMDIFF*, which automates all 4D-STEM/PNBD calculations. The current version of the program includes both entropy-based filtering and PSF deconvolution, various minor improvements and better documentation, and easier usage that requires just very minimal user input. Moreover, the original *STEMDIFF* scripts were rewritten and converted into a standardized distributable package, which can be installed from the official internet Python Package Index (PyPI; <https://pypi.org>; accessed on 15 November 2021). The improved 4D-STEM/PNBD method was applied to Au, TbF₃ and TiO₂ nanocrystals with two different crystalline modifications (anatase and rutile).

In all four cases, the crystals could be unambiguously identified and the resolution of the 4D-STEM/PNBD diffractograms was the same or even slightly better in comparison with the corresponding TEM/SAED patterns. We summarize that the current version of 4D-STEM/PNBD method can analyze polycrystalline samples in SEM microscopes in a fast and easy way, and the quality of the results is fully comparable with the standard TEM/SAED method.

2. Materials and Methods

2.1. Samples

Four nanocrystalline samples with various average crystal sizes were selected for testing of the improved 4D-STEM/PNBD method. In all four cases, the nanocrystals were deposited on a standard TEM copper grid coated with an electron-transparent carbon film. The first samples were Au nanoislands (size ~ 20 nm); their preparation was described in our previous study [17], in which they were employed as a nucleating agent for polypropylene. The second samples were small TbF₃ nanocrystals (size < 5 nm) with admixture of Gd³⁺, Yb³⁺ and Nd³⁺ ions that were designed as multimodal contrast agent for down- and upconversion luminescence, magnetic resonance imaging, and computed tomography [18]. The last two samples were commercial TiO₂ nanoparticles with two different crystalline modifications: anatase (average crystal size 25 nm) and rutile (average size 80 nm). Both anatase and rutile nanopowders were bought from Sigma-Aldrich (Prague, Czech Republic), dispersed in distilled water, sonicated (20 min) and a small droplet of the sonicated solution was put onto a carbon film and left to dry. The carbon-coated TEM grids with deposited nanoparticles were used for all following experiments.

2.2. TEM Characterization

All four samples (Au nanoislands [17], TbF₃ nanocrystals [18], TiO₂/anatase, and TiO₂/rutile) were thoroughly characterized by means of TEM microscopy (microscope Tecnai G2 Spirit Twin; FEI, Brno, Czech Republic; accelerating voltage 120 kV). Briefly, the nanocrystal morphology was visualized by bright field imaging (TEM/BF), elemental composition was assessed from energy-dispersive X-ray analysis (TEM/EDX) and crystalline structure was confirmed using selected-area electron diffraction (TEM/SAED). The final polycrystalline, powder TEM/SAED patterns were processed and converted to radially-averaged 1D-diffraction profiles by means of *ProcessDiffraction* program [16].

2.3. Calculation of PXR D Diffraction Patterns

The experimental TEM/SAED diffraction patterns were compared with theoretical powder X-ray diffractograms (PXR D). The PXR D diffractograms were calculated with program *PowderCell* [19]. The calculations were performed for perfect polycrystalline sample with random orientation of crystallites. The crystal structures for the calculation were obtained from the *Crystallography Open Database* [20].

2.4. 4D-STEM/PNBD Measurements and Calculations

2.4.1. SEM Microscope with Pixelated Detector

The 4D-STEM/PNBD method yields powder electron diffraction patterns by means of arbitrary SEM microscope equipped with a pixelated STEM detector. We employed a focused ion beam scanning electron microscope Helios G4 HP (FIB-SEM microscope; Thermo Fisher Scientific, Waltham, MA, USA) equipped with pixelated STEM detector T-pix (Thermo Fisher Scientific, Waltham, MA, USA), which was based on Timepix technology (DED detector with the array of 256 × 256 pixels, pixel size 55 μm and intensity detected in range 0–11,810 counts-per-pixel [21]). All measurements were performed at accelerating voltage of 30 kV; more details about the microscope can be found in our previous study [15].

2.4.2. Principle of 4D-STEM/PNBD Method

The principle of 4D-STEM/PNBD method is shown in Figure 1. The nanobeam diffraction patterns (NBD) and powder nanobeam diffraction patterns (PNBD) in Figure 1 come from the real measurement of sample TbF_3 (the sample is described in Section 2.1).

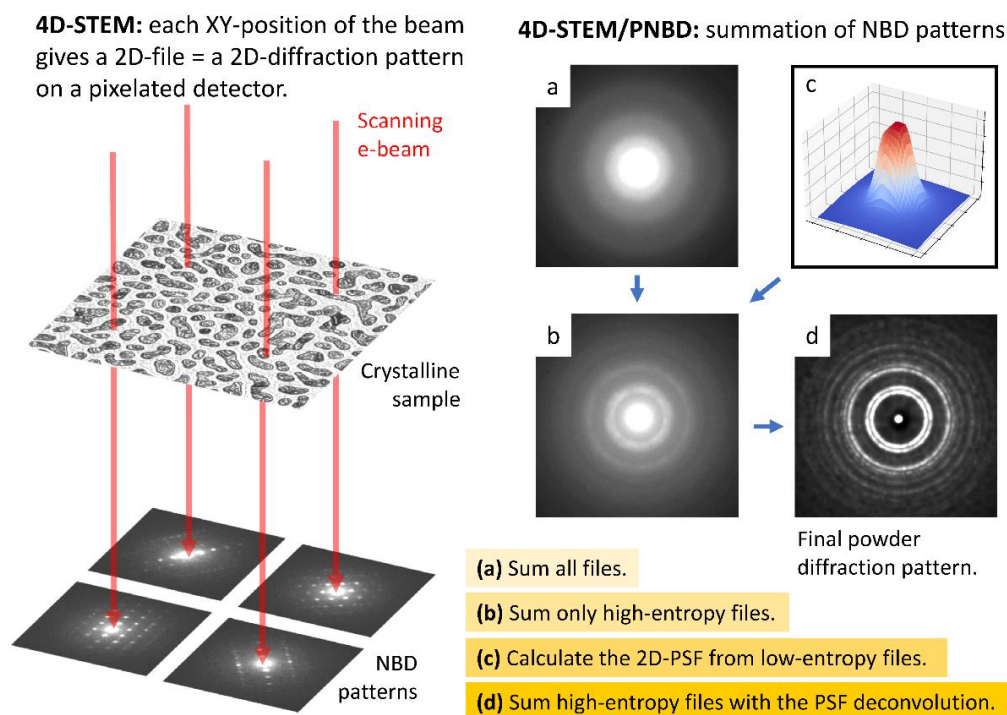


Figure 1. Principle of 4D-STEM/PNBD method. Left part of the image shows how the scanning electron beam penetrates through the sample and forms a set of nanobeam diffraction (NBD) patterns. Right part of the image shows how the individual NBD patterns can be combined into one powder nanobeam diffraction patterns (PNBD; with diffraction rings typical of the diffraction on polycrystalline samples): (a) PNBD obtained by the straightforward summation of all NBD patterns, (b) PNBD obtained by the summation of selected NBD patterns with high Shannon entropy values (high entropy indicated strongly diffracting crystals), (c) point spread function (PSF) calculated from low-entropy NBD patterns (the PSF represents the XY-spread of the primary beam), and (d) PNBD obtained by the summation of high-entropy NBD patterns with PSF deconvolution.

In a 4D-STEM measurement, the electron beam (primary beam) scans a 2D-array on a specimen and each XY-position of the beam gives a 2D-NBD pattern on pixelated detector (as shown schematically in left part of Figure 1). We note that Figure 1 shows just four beam positions and four corresponding NBD patterns for the sake of simplicity, while a typical scanning array during 4D-STEM measurements contains at least 2000 beam positions. The key step of 4D-STEM/PNBD method is the combination of the individual NBD's into the final PNBD pattern (as shown in the right part of Figure 1). The straightforward summation of all NBD patterns usually results in low-quality diffractograms, where diffractions are almost lost in the background noise and scattering of the amorphous carbon supporting film (Figure 1a). Better PNBD patterns are obtained if we sum just the NBD patterns containing strong diffractions (Figure 1b). The patterns with strong diffractions are selected from the dataset easily, as they exhibit high values of Shannon entropy [15]. Nevertheless, the best PNBD patterns are achieved if we calculate point spread function (PSF) of the primary beam (Figure 1c) from low-entropy NBD files and then we sum the high-entropy NBD patterns after the application of PSF deconvolution (Figure 1d). The implementation of PSF deconvolution is one of the key improvements of our 4D-STEM/PNBD method, as described and exemplified in this study.

2.4.3. 4D-STEM/PNBD Measurements

The 4D-STEM/PNBD method consists of two basic steps: 4D-STEM measurement (left part of Figure 1) and 4D-STEM/PNBD calculations (right part of Figure 1). The first step comprises three sub-steps: (i) the acquisition of standard STEM/BF micrograph in order to visualize the nanoparticles of interest, (ii) the definition of scanning array (scanning matrix) in the STEM/BF micrograph, from which we will obtain individual NBD patterns, and (iii) the 4D-STEM measurement itself, i.e., the point-by-point scanning of the selected 2D matrix and saving of the individual 2D-NBD diffractograms. The STEM/BF micrograph can be obtained either with a standard STEM detector (if available in a given system) or with the pixelated STEM detector (if we take the integral signal just from the central pixels of the detector, i.e., from the central circle with diameter ~ 30 pixels). The parameters for the 4D-STEM data collection can be defined conveniently with a control software of the pixelated detector. The key data collection parameters are the *scanning step* (=distance between two scanning points), *scanning matrix* (=area from which we will collect NBD diffractograms), and *exposure time* (=time per measurement of one NBD pattern). As for the *scanning step* parameter, we select optimal size according to the typical crystal size observed in STEM/BF micrograph: too small step would lead to multiple data collections from one crystal (redundant data) and too big step would result in too large scanning areas (which would force us to introduce corrections for possible beam shifts; in our systems the beam shifts were found to be insignificant on condition that the scanning area size $< 10 \mu\text{m}$). As for the *scanning matrix*, we usually use a rectangular array with at least 2000 points, but the shape can be arbitrary. As for the *exposure time*, we use simple trial-and-error method to set the time in such a way that the maximum intensity of the primary beam was slightly below the detector upper limit (i.e., 11,810 counts per pixel in the case of T-pix detector, as specified in Section 2.4.1). The correct exposure time setting is very important. Higher exposure times would not damage the detector, but the overflowed intensity of the central spot would prevent us from determining the precise primary beam shape (i.e., primary beam PSF in the XY plane) and, as a result, we could not perform the correct PSF deconvolution. Lower exposure times would result in weak diffractions, whose intensity might be too low for the correct background subtraction. The parameters of data collections used in this study are given in Table 1.

Table 1. Data acquisition settings.

Dataset ID	Step ¹ [nm]	Scanning Matrix ²	HFW ³ [μm]	WD ⁴ [mm]	Probe Current [pA]	Total No. of Files	Duration [h:m:s]
Au	20	9×230	4.6	5.4	25	2070	0:05:30
TbF ₃	50	12×190	9.5	4.8	25	2280	0:06:20
TiO ₂ /anatase	25	20×100	2.5	3.2	13	2000	0:10:30
TiO ₂ /rutile	25	20×100	2.5	3.2	13	2000	0:10:30

¹ Step = scanning step = distance between two scanning points. ² Scanning matrix = rectangular XY array of measurement points. ³ HFW = Horizontal field width = real width of the STEM/BF image. ⁴ WD = Working distance = distance between electron column pole-piece and sample.

Additional technical details concerning the measurement can be found in our previous work [15]. Once the measurement parameters are set, the final 4D-STEM measurement is performed automatically using the simple control software coming with the pixelated detector. During the measurement, the individual diffraction patterns are saved one-by-one to the selected directory in the form of binary files and the whole data collection time usually does not exceed 12 min.

The second step of 4D-STEM/PNBD method—the summation of the individual NBD patterns in order to obtain the final PNBD pattern—has been automated by means of our freeware program package called STEMDIFF. The details are given below in the Results section, as the updated STEMDIFF package is one of the significant outputs of this work, and, more importantly, the data processing is closely associated with the final results. Here we just briefly summarize that the updated STEMDIFF package requires a minimal

user input and performs all types of summations, i.e., the direct summation of all NBD files (Figure 1a), the summation of selected, high-entropy NBD files (Figure 1b), and the summation of high-entropy files with PSF deconvolution (Figure 1c,d). The final 4D-STEM/PNBD diffraction patterns (Figure 1a,b,d) can be processed with arbitrary software for powder diffraction pattern analysis. The most straightforward option is to process the 4D-STEM/PNBD patterns with the same software that is used for the analysis of TEM/SAED patterns, such as the well-established *ProcessDiffraction* program (for the processing of experimental powder electron diffraction patterns [16]) and *PowderCell* program (for the calculation of theoretical powder X-ray diffraction patterns [19]).

3. Results

3.1. Results of the Improved 4D-STEM/PNBD Method

The improved 4D-STEM/PNBD method was applied on four samples. The first two samples (Au nanoislands and TbF_3 nanoparticles) had already been studied with the previous version of 4D-STEM/PNBD and we tested how the results could be improved with the current version of the method. The last two samples (TiO_2 nanoparticles with different crystalline modifications—anatase and rutile) were newly prepared in order to demonstrate that the 4D-STEM/PNBD method could distinguish samples with identical chemical composition.

3.1.1. Au Nanoislands: Strongly Diffracting Nanocrystals

The TEM and 4D-STEM/PNBD results for Au nanoislands are summarized in Figure 2. The Au nanoislands on thin carbon film (Figure 2a) represent quite large nanocrystals, which exhibited very strong diffractions not only in TEM/SAED pattern (Figure 2b), but also in 4D-STEM/PNBD pattern calculated without PSF deconvolution (Figure 2c).

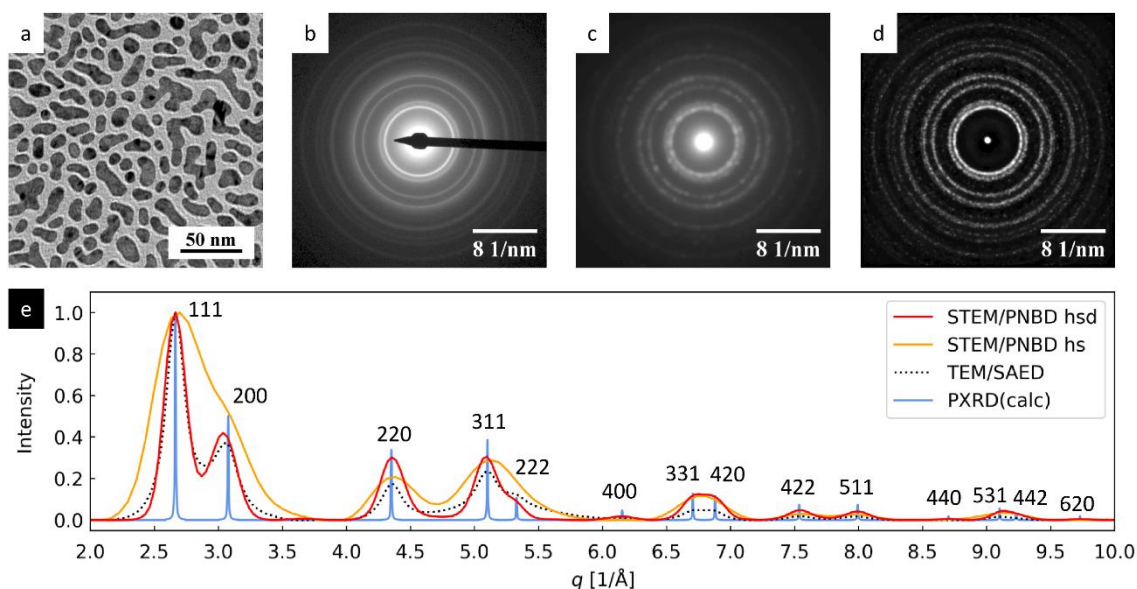


Figure 2. 4D-STEM/PNBD results for Au nanoislands and their comparison with TEM and PXRD results: (a) TEM/BF image, (b) TEM/SAED diffraction pattern, (c) 4D-STEM/PNBD diffraction pattern calculated without PSF deconvolution, (d) 4D-STEM/PNBD pattern calculated with PSF deconvolution, and (e) comparison of radially averaged profiles from 4D-STEM/PNBD patterns with deconvolution (red line), 4D-STEM/PNBD without deconvolution (orange line), TEM/SAED (black dotted line), and theoretically calculated PXRD diffraction pattern of Au (blue line). All 4D-STEM/PNBD diffractograms and profiles in this figure were calculated for high-entropy files (20% of datafiles with the highest values of Shannon entropy as described in Section 2.4.2). The abbreviation *hs* and *hsd* in the plot legend mean calculation with high-entropy files (*hs*) and calculation with high-entropy files and PSF deconvolution (*hsd*), respectively.

We processed the Au dataset with the recent version of 4D-STEM/PNBD method in order to demonstrate how it can improve the results in the case of strongly diffracting nanocrystals. In the first step, we reproduced the calculation from our previous study (i.e., we used the newly measured dataset and updated software, but we did not employ PSF deconvolution) and the resulting 4D-STEM/PNBD diffractogram was quite comparable to TEM/SAED (cf. Figure 2b,c). Nevertheless, the PSF deconvolution yielded even better diffractogram, with stronger and sharper diffraction rings (Figure 2d).

The improvement of the 4D-STEM/PNBD results due to PSF deconvolution is best documented on 1D-diffraction profiles (Figure 2e). The standard PNBD calculation (i.e., summation without PSF deconvolution; orange line) gave reasonable diffractogram (orange line), corresponding to theoretical PXRD pattern (blue line), but the resolution (i.e., the diffraction widths) was definitely worse in comparison with TEM/SAED (black dotted line). The PNBD calculation with PSF deconvolution (red line) yielded the diffraction pattern, in which the diffraction intensities and resolution were even slightly better than in the case of TEM/SAED (namely in the region of high-angle diffractions with $q > 5 \text{ \AA}^{-1}$). This could be attributed to a positive side effect of PSF deconvolution, which decreases the background intensity and improves signal-to-noise ratio (compare Figure 2b–d).

3.1.2. TbF₃ Nanoparticles: Smaller Nanocrystals with Preferred Orientation

The results for TbF₃ nanoislands are summarized in Figure 3. The TbF₃ nanocrystals (Figure 3a) were small and tended to form agglomerates. They exhibited strong diffractions in TEM/SAED (Figure 3b), but their 4D-STEM/PNBD pattern calculated without PSF deconvolution showed quite weak and broad diffraction rings (Figure 3c).

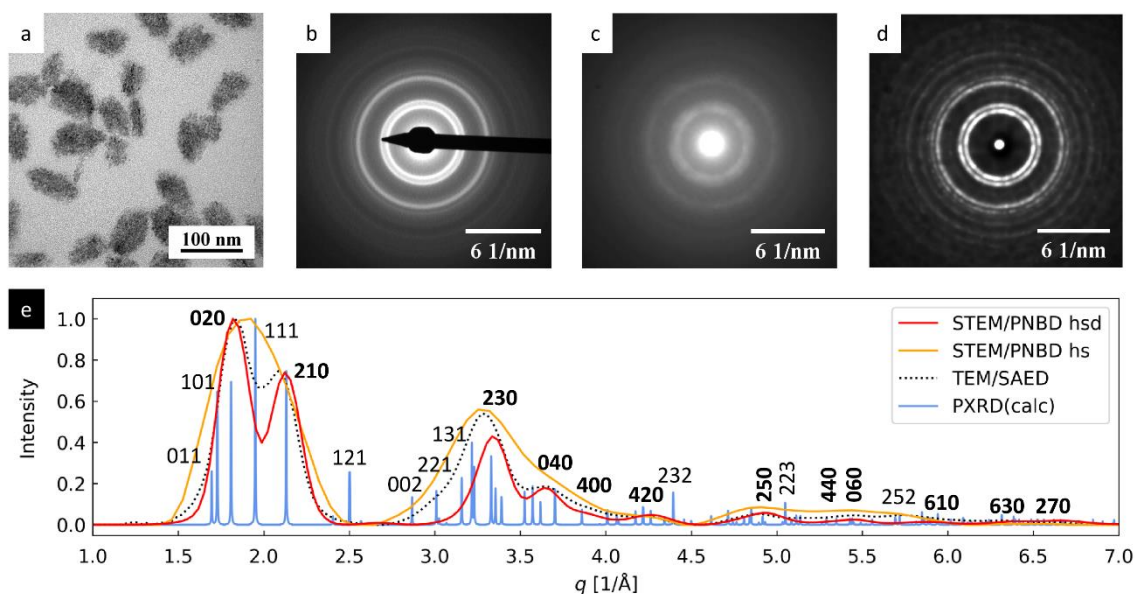


Figure 3. 4D-STEM/PNBD results for TbF₃ nanocrystals and their comparison with TEM and PXRD results: (a) TEM/BF image, (b) TEM/SAED diffraction pattern, (c) 4D-STEM/PNBD diffraction pattern calculated without PSF deconvolution, (d) 4D-STEM/PNBD pattern calculated with PSF deconvolution, and (e) comparison of radially averaged profiles from 4D-STEM/PNBD patterns with deconvolution (red line), 4D-STEM/PNBD without deconvolution (orange line), TEM/SAED (black dotted line), and theoretically calculated PXRD diffraction pattern of TbF₃ (blue line). All 4D-STEM/PNBD diffractograms and profiles in this figure were calculated for high-entropy files (20% of datafiles with the highest values of Shannon entropy as described in Section 2.4.2). The abbreviation *hs* and *hsd* in the plot legend mean calculation with high-entropy files (*hs*) and calculation with high-entropy files and PSF deconvolution (*hsd*), respectively.

The weaker diffraction power of TbF₃ nanoparticles in 4D-STEM (Figure 3c) was connected with their smaller size (weaker diffractions from the individual crystals relative to the supporting carbon film, whose scattering is non-negligible for lower energy SEM

electrons) and agglomeration (higher absorption of lower-energy SEM electrons within the agglomerates). Nevertheless, the recalculation of optimized TbF₃ dataset with the new version of STEMDIFF package exhibited even higher improvement of the final powder diffraction pattern than in the case of strongly diffracting Au nanoislands—the diffractions much stronger, and the final diffractogram was much closer to the results from TEM/SAED (compare Figure 3b–d).

In analogy with the Au nanoislands, the positive effect of the improved 4D-STEM/PNBD method on the TbF₃ diffraction pattern is best seen from the comparison of the 1D radially averaged diffraction profiles (Figure 3e). The calculation without PSF deconvolution (orange line) was sufficient to identify the TbF₃ crystalline structure as the peak positions and intensities corresponded quite well to the TEM/SAED profile (black dotted line), but the resolution was rather low (just three broad maxima with weak shoulders at $q \approx 1.8$, 3.3 and 5.2 Å⁻¹). The calculation with PSF deconvolution (Figure 3e, red line) yield much better results: the first original broad peak (orange line, $q \approx 1.8$ Å⁻¹) was split into two sharp diffractions, the second peak (orange line, $q \approx 3.3$ Å⁻¹) was split to three diffractions, and the third low-intensity peak was split in three distinct maxima as well. Moreover, the PSF-deconvoluted profile showed an additional pair of very low intensity peaks at the highest diffraction angles (red line, $q \approx 6.5$ Å⁻¹). The resolution of the improved 4D-STEM/PNBD calculation was even slightly better in comparison with TEM/SAED (cf. red and black-dotted lines in Figure 3e).

The difference between the calculated PXRD pattern (Figure 3e, blue line) and all electron diffraction patterns (black, orange and red lines) was associated with strong preferred orientation (PO) of TbF₃ nanocrystals, as explained elsewhere [18]. Briefly, the PXRD diffraction pattern was calculated for ideal, randomly oriented, isometric TbF₃ nanocrystals, while real TbF₃ synthesis resulted in thin nanoplatelets, most of which laid on their small facets oriented in such a way that their shortest unit cell parameter, *c*, was parallel with the electron beam [18]. This corresponded to the PO of the nanocrystals with zone axis [*uvw*] = [001]. Consequently, the Weiss zone law (WZL: $hu + kv + lw = 0$, where *h*, *k*, *l* are diffraction indexes and *u*, *v*, *w* are the indexes of the zone axis [22]) took quite simple form ([*uvw*] = [001] ⇒ $hu + kv + lw = h0 + k0 + l1 = 0$ ⇒ $l = 0$), indicating that the strongest diffraction peaks should be of the type [*hk*0]. Indeed, the experimental TEM/SAED and 4D-STEM/PNBD diffraction patterns (representing the real TbF₃ nanoplatelets with strong PO) showed stronger *hk*0 diffractions (such as 020, 210 and 230) and weaker *hkl* diffractions (such as 111, 121 and 232) in comparison with the theoretically calculated PXRD diffraction pattern (representing the ideal crystals with random orientation). The small shift of the diffraction at $q \approx 3.3$ Å⁻¹ to the right after PSF deconvolution (red line vs. orange line in Figure 3e) could be attributed to the strong PO of TbF₃ nanocrystals as well: the lower background after the deconvolution (cf. Figure 3b,d) lead to sharper and more precisely defined peak, whose maximum was shifted towards diffraction 230, in agreement with the WZL, as described above. The theoretical possibility that the shift might be a deconvolution artifact, is discussed below in Section 4.3.

3.1.3. TiO₂ Nanoparticles: Differentiation between Anatase and Rutile Modifications

The last two systems (TiO₂ nanoparticles with two different crystalline modifications, anatase and rutile) were selected in order to demonstrate that the 4D-STEM/PNBD method can reliably distinguish nanocrystals with the identical chemical composition, but different crystalline structure. For the sake of brevity, Figure 4 summarizes just the final, radially averaged 1D diffraction profiles. For both anatase (Figure 4a) and rutile (Figure 4b), the agreement between theoretically calculated PXRD diffractograms (Figure 4, blue lines), experimental TEM/SAED diffractograms (Figure 4, black dotted lines) and experimental 4D-STEM/PNBD diffractograms calculated with PSF deconvolution (Figure 4, red lines) was very good. The intensity and resolution of diffractions in TEM/SAED and 4D-STEM/PNBD were almost identical. This confirmed the reliability and reproducibility of our improved 4D-STEM/PNBD method. The main conclusion was that the improved

version of 4D-STEM/PNBD method could be employed in fast and easy identification of different nanocrystals with similar or even identical composition, which is impossible with other methods available in an SEM microscope.

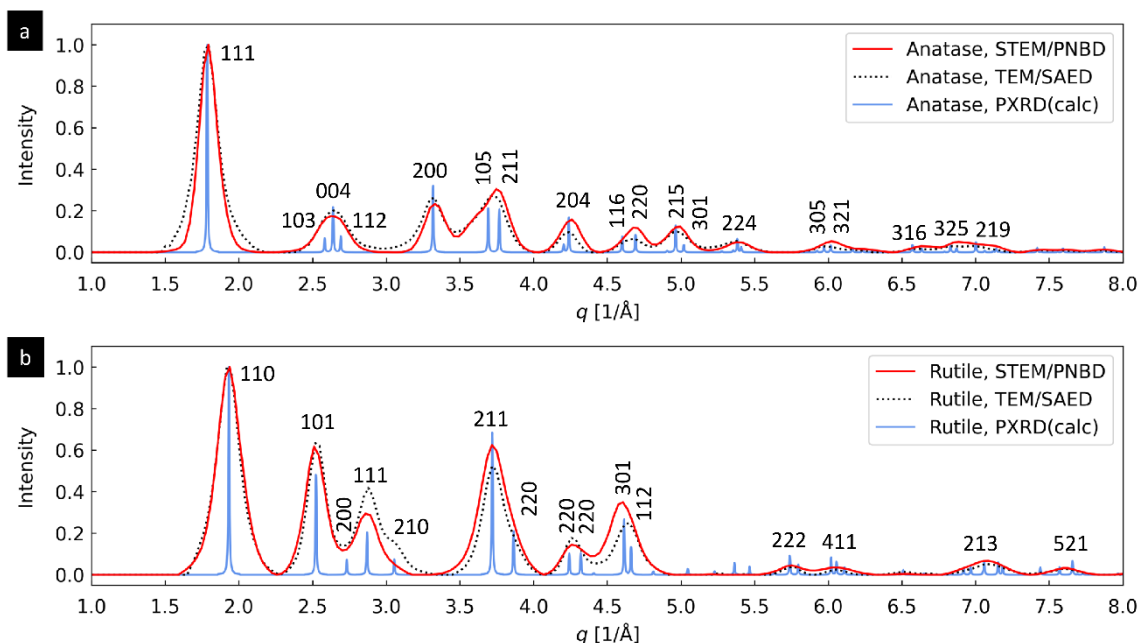


Figure 4. Comparison of 4D-STEM/PNBD, TEM/SAED and PXRD results for TiO_2 nanocrystals with two different crystalline modifications: (a) anatase and (b) rutile. The 4D-STEM/PNBD results (red lines) were calculated with the recent version of the method including PSF deconvolution. The TEM/SAED results (black dotted lines) and PXRD results (blue lines) were obtained as described above (Section 2.1).

3.2. Description of the Improved STEMDIFF Package

The freeware STEMDIFF program package converts the 4D-STEM dataset into 2D- and 1D-powder diffraction patterns, requiring just minimal user input. The substantially improved version of STEMDIFF, which was developed within this work, includes automatic entropy-based filtering, PSF deconvolution and many other improvements, such as the radial averaging of the final 2D diffraction pattern to the 1D diffraction profile. The final 1D diffractogram can be compared with the powder diffractograms from various databases, calculations and/or X-ray diffraction experiments. In the following subsections, we describe the basic STEMDIFF algorithm (Section 3.2.1) and the STEMDIFF user interface (Section 3.2.2), while the appendixes give information about the installation and efficient usage of the Python version of the package (Appendix A) and basic information about MATLAB version of the package (Appendix B).

3.2.1. STEMDIFF Algorithm

The principal part of STEMDIFF algorithm is outlined in Figure 5. The scheme shows real data and outputs from the calculation of TbF_3 nanocrystals (Section 3.1.2). The program always starts with a reading of a 4D-STEM dataset, i.e., with the reading of a 2D array of 2D diffractograms (2D nanobeam diffraction patterns, NBD) that are saved in the form of binary files (Figure 5a). The first processing route consists of a straightforward summation of all files (Figure 5b), but for most samples this is insufficient and the final radially averaged 1D-profiles (Figure 5c) contain broad, low-intensity peaks that are very hard to separate from the background.

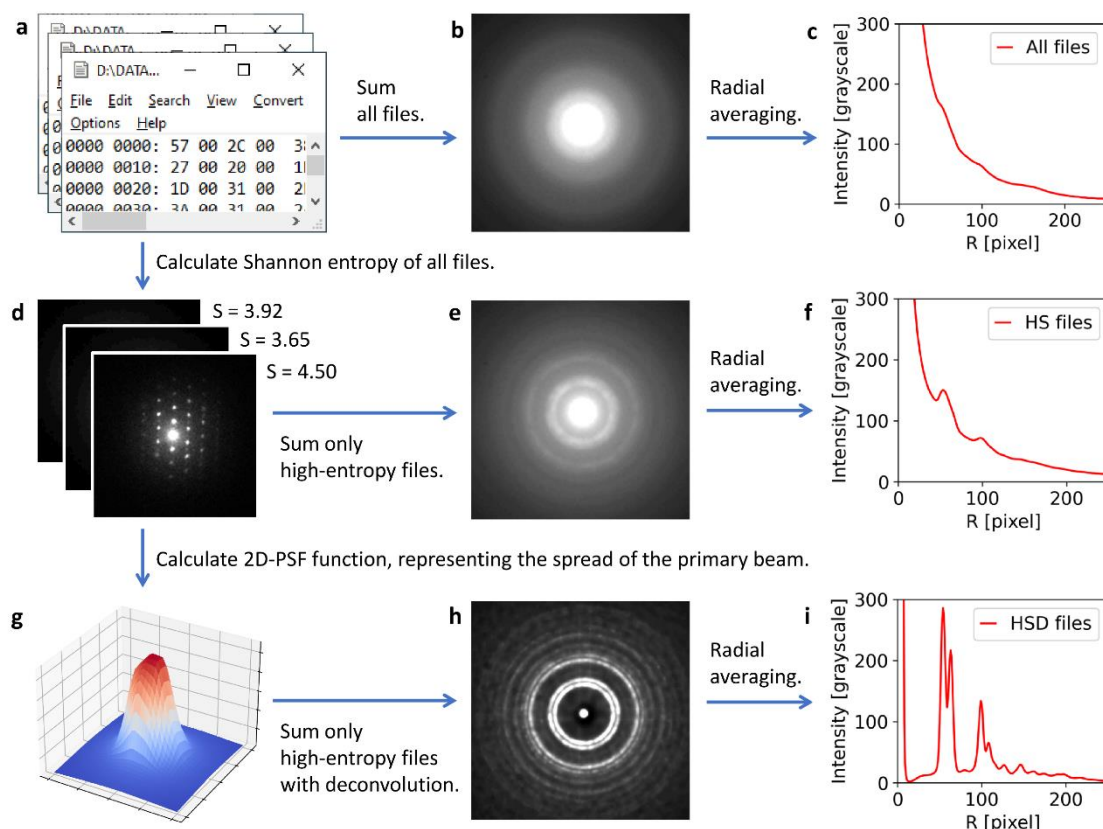


Figure 5. Scheme of STEMDIFF algorithm. The first processing route (a–c) is the straightforward summation of all files that contain the individual nanobeam diffraction patterns (b), but the final diffraction profiles contain very broad, low-intensity diffraction peaks (c). The second processing route (d–f) employs entropy-based filtering (d) and summation of just high-entropy files containing strong diffractions (e), which results in well-defined diffraction peaks, although their intensity and resolution is still suboptimal (f). The third processing route (g–i) includes determination of PSF, which represents the XY-spread of the primary beam (g), and application of PSF deconvolution to high-entropy files before their summation (h), which results in substantially sharper peaks with higher resolution and lower background (i).

The better processing of 4D-STEM/PNBD data employs entropy filtering: the program calculates Shannon entropy [23,24] of all files (Figure 5d), then it sums only the high-entropy files (Figure 5e), and after radial averaging we get well-defined peaks (Figure 5f). The principle of entropy-based filtering is illustrated in Figure 6: the lowest-entropy files contain just the central spot corresponding to the primary beam (Figure 6, upper left corner), with the increasing value of Shannon entropy (S) the files contain more-and-more diffraction spots (Figure 6, files with intermediate S values), and the highest-entropy files contain a high number of strong diffractions (Figure 6, lower right corner). The entropy-based filtering was the key part of the previous version of STEMDIFF package, which yielded 4D-STEM/PNBD diffractograms that were (after a careful background subtraction) comparable to TEM/SAED, although their resolution was somewhat lower [15].

The best processing of 4D-STEM/PNBD data, which has been included in the improved version of STEMDIFF package within this work, is based on PSF deconvolution: the program employs the lowest-entropy files in order to calculate 2D-PSF, which represents the XY-spread of the primary beam (Figure 5g). Then the program calculates PSF deconvolution of the individual high-entropy files before their summation (Figure 5h). After this treatment, the final radially averaged profiles contain sharp, high-intensity diffraction peaks (Figure 5i), whose resolution is fully comparable with the peaks from TEM/SAED, as exemplified in Section 3.

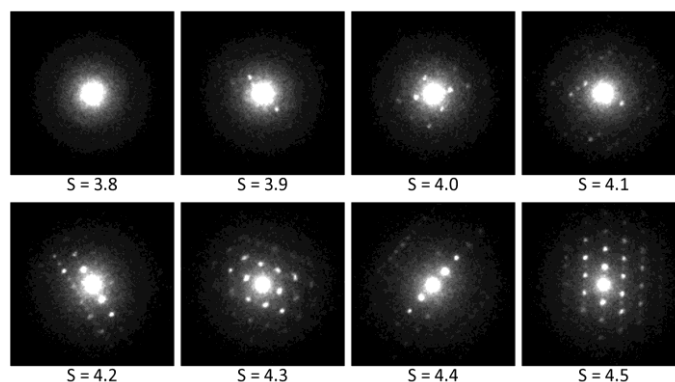


Figure 6. Entropy-based filtering: the datafiles with high Shannon entropy (S) contain strong diffraction peaks and *vice versa*.

3.2.2. STEMDIFF User Interface

The user interface of the recent version of STEMDIFF package is shown in Figure 7. The improved STEMDIFF package was developed as a part of this work. As illustrated in Figure 7, the current version of the package uses freeware Spyder integrated development environment (IDE) as a simple user interface (UI).

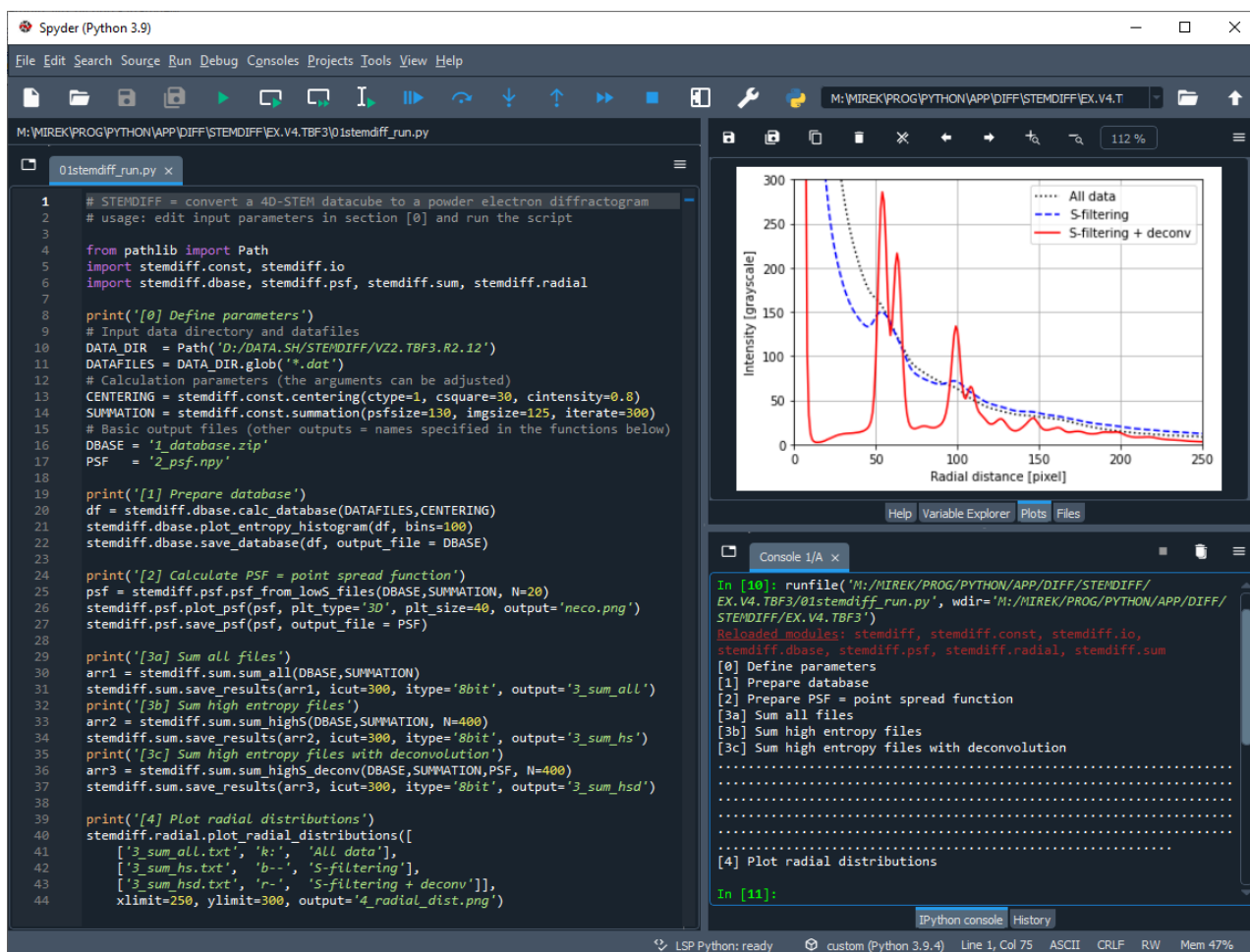


Figure 7. User interface of STEMDIFF package.

STEMDIFF package is focused on fast, easy and routine everyday use. The user just copies a template Python script (shipped within the program package) to Spyder

(left pane in Figure 7) and modifies two key input parameters at the beginning of the script: the name of the directory with the input files and the number of iterations during PSF deconvolution. Optionally, it is possible to fine-tune some parameters that control the centering (i.e., finding the center of individual diffractograms) and summation, as described in Appendix A. When the script is run (Figure 7, green triangle in menu bar), the textual outputs are shown in Console window (Figure 7, lower right pane), and the final 1D-diffraction profile is shown in the Plots window (Figure 7, upper right pane). Other outputs (such as the 2D PNBD diffraction patterns shown in Figures 2, 3 and 5) are saved automatically in the current directory (i.e., in the directory with the modified template script).

3.3. Influence of Experimental and Processing Parameters on 4D-STEM/PNBD Results

3.3.1. Data Processing Parameters: Summation and Deconvolution

Surprisingly enough, the data processing parameters exhibit a stronger influence on the quality of the 4D-STEM/PNBD diffractograms than the experimental parameters. In other words, if the data collection parameters are reasonable, the decisive factor influencing the final intensity and resolution of the diffractions is the way of summation and deconvolution within STEMDIFF package. This is illustrated in Figures 8 and 9, which show final 1D-profiles of Au and TbF_3 samples. For both samples, the data collection parameters (scanning step, scanning matrix, exposure time, etc.) were carefully optimized according to the recommendations summarized in Section 2.4.3. However, in both cases, the intensities and resolution of the diffractions were dramatically influenced by the summation type (Figure 8) and number of the deconvolution iteration cycles (Figure 9).

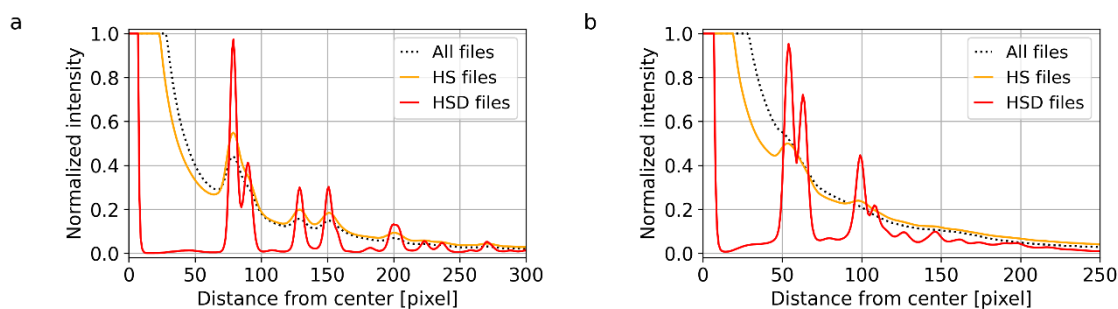


Figure 8. Influence of the summation type on the quality of 4D-STEM/PNBD results for (a) Au nanoislands and (b) TbF_3 nanocrystals. Both plots show final 1D-diffraction profiles from STEMDIFF calculation. STEMDIFF package can sum all files (black dotted line), high-entropy files (HS files; orange line), or high-entropy files with PSF deconvolution (HSD files, red line).

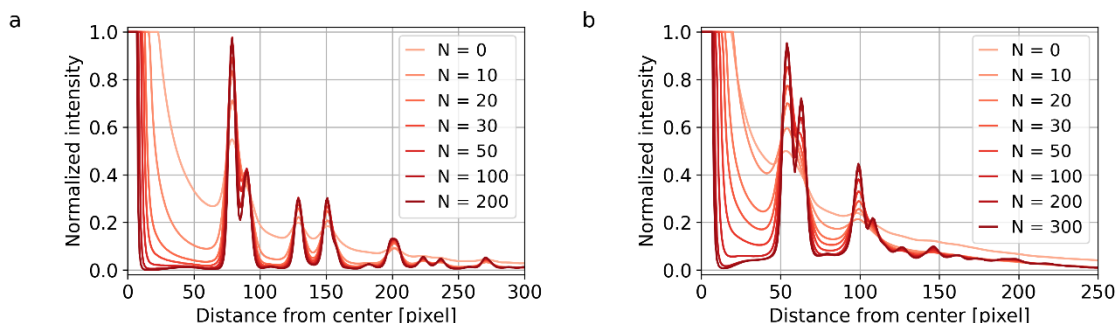


Figure 9. Influence of the number of iteration cycles, N , during PSF deconvolution on the quality of 4D-STEM/PNBD results for (a) Au nanoislands from Section 3.2.1 and (b) TbF_3 nanocrystals from Section 3.2.2. Both plots show final 1D-diffraction profiles from STEMDIFF calculation.

For the strongly diffracting Au nanoislands (Figures 8a and 9a), the influence of the processing parameters was slightly lower (i.e., for this almost ideal sample we could get reasonable results even without entropy-based filtering and/or PSF deconvolution).

Nevertheless, even in this case, the enhancement of peaks after deconvolution (Figure 8a), and with the increasing number of deconvolution iterations (Figure 9a) was strong and evident. The optimal number of deconvolution cycles was around 200, as the difference between 100 and 200 cycles (Figure 9a) was quite small and further deconvolution cycles just prolonged the computation time without apparent benefit.

For TbF₃ nanoparticles with somewhat weaker diffractions (Figures 8b and 9b), the straightforward summation of all NBD patterns without the entropy filtering and PSF deconvolution (Figure 8b, dotted line) yielded very broad and low-intensity peaks, which were almost impossible to separate from the background. The summation of just 20% of the files with the highest entropy (Figure 8b, orange line) resulted in two clear peaks (around 50 and 100 pixels from the center) and one very broad peak (ranging from ca 120 to 200 pixels from the center); this result was far from ideal, but sufficient for TbF₃ identification (as documented in Figure 3e). The summation of high-entropy files after application of PSF deconvolution (Figure 8b, red line) enhanced both the intensity and resolution of the peaks drastically. The optimal number of deconvolution cycles for TbF₃ nanocrystals (ca 300) was higher than for Au nanoislands (ca 200), which seems to be a general trend—lower diffracting samples require more deconvolution cycles.

3.3.2. Experimental Parameters: Primary Beam Intensity and Exposure Time

The intensity of the primary beam and the exposure time are important parameters influencing 4D-STEM/PNBD results as illustrated in Figure 10. The measurement can be set in two principal ways: (i) non-overflowed intensity of the diffractions (Figure 10a–c) or (ii) non-overflow intensity of the primary beam (Figure 10d–f).

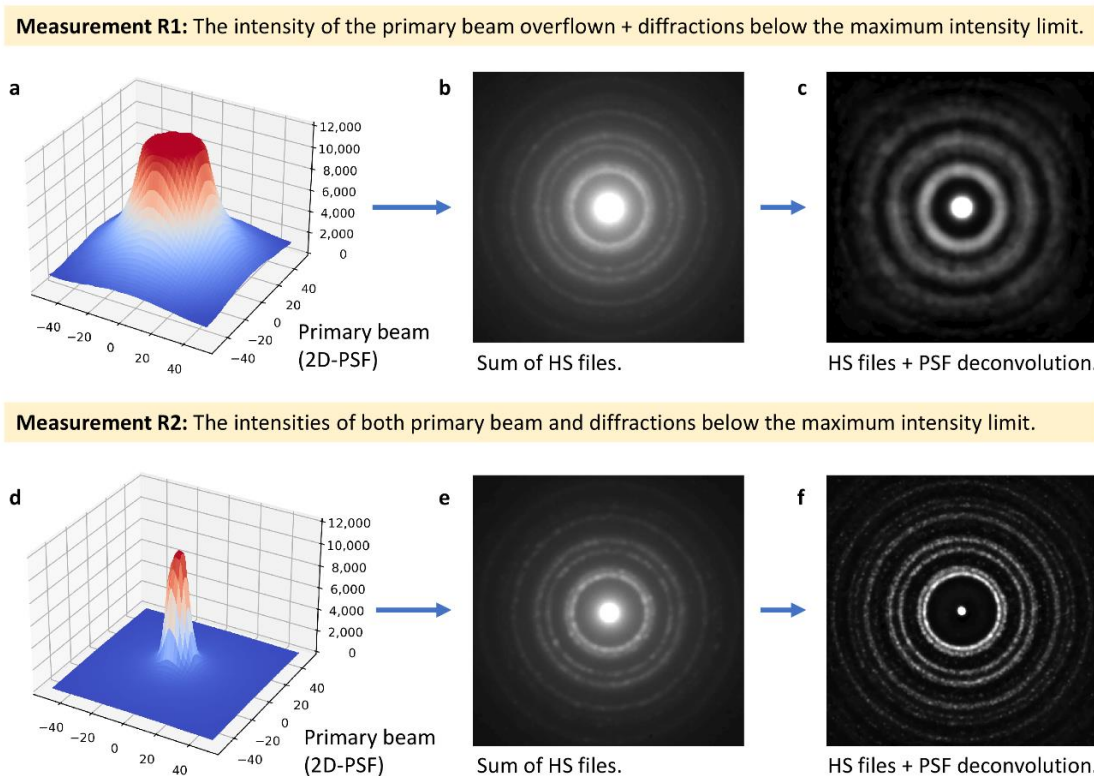


Figure 10. Influence of the measurement type on the quality of 4D-STEM/PNBD results for Au nanoislands. Measurement R1 (upper row) employs high exposure times, which results in (a) an overflowed primary beam and (b) higher intensity diffractions, but (c) wrong PSF deconvolution results. Measurement R2 (lower row) employs lower exposure time, which leads to (a) a non-overflowed intensity of the primary beam and (b) lower intensity of diffractions, but (c) correct PSF deconvolution results. All data shown in the figure come from the measurements of Au nanoislands. Measurement R1 (a–c) was made in our previous study [15], while the optimized measurement R2 (d–f) was carried out within this work.

The measurement of the first type (i.e., measurement R1; Figure 10a–c) was used in our previous work [15]. The maximal measurable intensity of our pixelated detector (I_{MAX}) was 11,810 counts per pixel. The exposure time was adjusted in order to maximize intensities of diffracted beams while keeping them below I_{MAX} . Under these conditions, the primary beam on the detector overflowed (Figure 10a) and the summation of entropy-filtered files gave strong diffractions (Figure 10b). Nevertheless, it was not possible to reconstruct the correct XY-shape of the primary beam due to its overflowed intensity (Figure 10a: the intensity was cut and the non-Gaussian shape of the primary beam after passing through the supporting carbon film could not be interpolated reliably). Therefore, the final summation with the PSF deconvolution failed to yield sharp diffractions (Figure 10c).

The optimized measurement of the second type (i.e., measurement R2; Figure 10d–f) was introduced in this study. The exposure time was adjusted so that the intensity of the primary beam was below I_{MAX} (Figure 10d). Consequently, the diffracted beams were somewhat weaker (Figure 10e) in comparison with measurement R1 (Figure 10b). On the other hand, it was possible to get the correct PSF of the primary beam and, as a result, the final summation including both entropy filtering and deconvolution (Figure 10f) gave much better results than measurement R1 (Figure 10c), which was the main advantage of the improved 4D-STEM/PNBD method.

3.3.3. Experimental Parameters: Dataset Size

The effect of the dataset size on the quality of final 4D-STEM/PNBD diffraction patterns was quite small. This is illustrated in Figure 11 that shows the 1D-diffraction profiles of Au nanoislands. The diffraction profiles come from the simple summation of all files in order to eliminate possible effect from entropy filtering or PSF deconvolution. Figure 11 evidences that the final 1D diffraction profiles were almost independent on the number of datafiles for both high (Figure 11a) and low exposure times (Figure 11b).

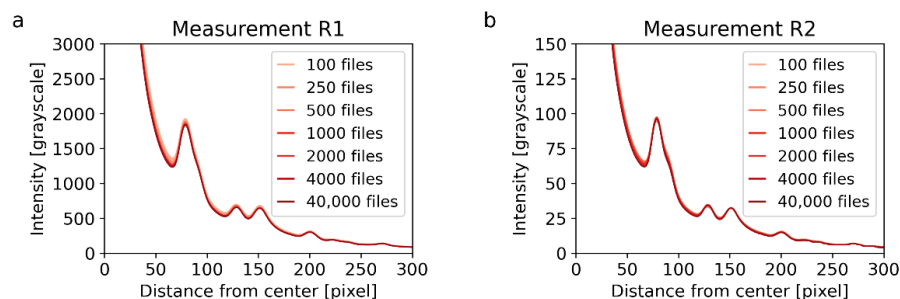


Figure 11. Influence of the dataset size on the quality of 4D-STEM/PNBD results. Both plots show 1D-diffraction profiles of Au nanoislands after summation of all files (i.e., entropy filtering and PSF deconvolution were not included in the calculation in order not to influence the results). The plots show the results of measurements R1 (a) and R2 (b). The measurements R1 and R2 differ by the exposure time as explained in Section 3.3.2 and illustrated in Figure 10.

4. Discussion

4.1. Originality and Novelty of 4D-STEM/PNBD Method

According to the available literature, which was summarized in the Introduction, our 4D-STEM/PNBD method is different from the existing 4D-STEM methods in three main aspects. At first, a great majority of other 4D-STEM methods have been developed in the field of transmission electron microscopy (4D-STEM-in-TEM; [8] and references therein), while our method is focused on scanning electron microscopy (4D-STEM-in-SEM; [15] and references therein). At second, the so-far-described 4D-STEM-in-SEM methods have been based on older, bulky CCD and CMOS detectors (which required rather non-standard hardware adjustments of SEM microscopes [11–14]), but our method relies on a modern, small DED detector (which can be installed to any modern SEM microscope with a standard port for STEM [10]). At third, both 4D-STEM-in-TEM and 4D-STEM-in-SEM

methods found in the literature have been focused on the analysis of all individual NBD patterns of the 4D-dataset (which requires special software and special crystallographic knowledge [8,9,25]), but our method combines the individual NBD patterns into one simple PNBD pattern (which can be processed with standard, well-established, easy-to-use programs such as *PowderCell* [15,16,26] or *VESTA* [27]). Moreover, we have developed simple software requiring just a minimal user input (STEMDIFF package; Section 3.2), which automatically performs the summation of all individual NBD patterns in order to obtain the high-resolution PNBD pattern.

The focus of our 4D-STEM/PNBD method on powder diffraction analysis is its most distinctive feature. In TEM, some analogy of 4D-STEM/PNBD might have been developed and employed as well, but the standard, simpler and faster TEM/SAED method yields identical results directly (as exemplified in Section 3.1). Therefore, the 4D-STEM-in-TEM developers and users aim at analysis of the individual NBD patterns, although the possibility of combining selected NBD patterns into a powder diffractogram is occasionally mentioned and/or employed in calibration [9]. In SEM, some authors tested direct recording of PNBD patterns by means of special set of annular limiting apertures [11] or simple straightforward summation of individual NBD patterns during scanning [14], but our results showed unambiguously that this could work only for the nanocrystals with extremely strong diffractions (such as Au nanoislands in Figure 8a) and fails for systems containing smaller crystals (such as TbF₃ in Figure 8b—note that the black dotted line representing the direct summation of NBD patterns does not show any distinct diffraction peaks). The difference between the traditional approach (straightforward summation of all files) and the recent version of 4D-STEM/PNBD method (optimized data collection combined with summation of high-entropy files with PSF deconvolution) is evident from the introductory Figure 1 as well: the traditional summation of all files from TbF₃ dataset yielded just very broad, low-intensity diffraction peaks (Figure 1a), while the improvements introduced in the STEMDIFF package resulted in sharp, high-intensity diffractions (Figure 1d). Further analysis of the final, radially averaged 4D-STEM/PNBD diffraction patterns proved that their resolution is fully comparable or even slightly better in comparison with the common TEM/SAED diffractograms (Sections 3.1.1–3.1.3).

4.2. Advantages and Disadvantages of 4D-STEM/PNBD Method

As already emphasized in the introduction (Section 1) and description of STEMDIFF package (Section 3.2), the whole 4D-STEM/PNBD method is focused on a simple and routine everyday use. Nevertheless, the simplicity comes at certain cost. The reduction of the whole 4D-STEM dataset into a single 1D-powder diffractogram greatly simplifies data interpretation, but the information about the orientation of the individual nanocrystals within the sample is lost.

The main **advantages** of 4D-STEM/PNBD method are connected with its simplicity. We do not force potential users to analyze every single 2D-NBD pattern within the 2D-scanning array in order to get basic crystallographic information about the investigated sample. Instead, it is enough to perform substantially simpler analysis of one, averaged PNBD profile. Moreover, the final diffraction profile is obtained by means of a small, easy-to-understand Python script within freeware, easy-to-install STEMDIFF program package. This brings the following benefits:

- *Ease of use*: The measurement of 4D-STEM dataset in a modern SEM microscope with modern software is a routine task. The conversion of 4D-STEM data to 1D-powder diffractogram is performed automatically with freeware STEMDIFF package. The final analysis of a single 1D-powder electron diffractogram is usually quite easy as explained in the following item.
- *Accessible to everyone*: The method can be used by virtually anyone with basic SEM experience and elementary computer skills. The analysis of powder electron diffraction pattern is basically a fingerprint method consisting of three steps: (i) the obtaining experimental diffractogram by means of 4D-STEM/PNBD method as described above

in Section 3.2, (ii) the simple calculation of the theoretical PXRD diffractogram of the analyzed sample by means of arbitrary free software, such as *PowderCell* [19] or *VESTA* [27], and (iii) the comparison of the results. If the experimental and theoretical diffractograms correspond to each other (such as those in Figures 2–4), the crystal structure is identified.

- *The conversion of an SEM microscope to a powder diffractometer:* This opens quite new possibilities for SEM users. Standard SEM methods include imaging (with secondary, backscattered or transmitted electrons) and elemental analysis (such as energy-dispersive analysis of X-rays). A simple diffraction technique in an SEM microscope, equivalent to TEM/SAED, has been missing so far. The 4D-STEM/PNBD method aims to fill this gap as it enables to identify crystal structures of nanocrystalline powders like in the field of TEM microscopy.

The disadvantage of 4D-STEM/PNBD method results from the fact that it does not consider the additional information contained in the individual NBD patterns. More precisely, we use the individual NBD patterns just for the summation that yields the final PNBD pattern, while ignoring the specific positions and intensities of diffraction spots at each sample location. As the diffraction spots carry the information about the structure and orientation of the investigated material at a given location, the 4D-STEM/PNBD method cannot solve some special problems that are typically addressed by 4D-STEM-in-TEM methods, such as the visualization of different materials in the nanoscale (virtual imaging [28]), the identification of individual phases (structural classification [29]), the analysis of orientation of the individual nanocrystals (orientation mapping [30]), the analysis of strains of the individual nanocrystals (strain mapping [31]) and the enhancement of resolution and/or contrast of the micrographs by means of some advanced techniques (differential phase contrast or ptychography [32]). This is the price paid for the 4D-STEM/PNBD straightforwardness and simplicity.

4.3. Possible Artifacts on 4D-STEM/PNBD Diffractograms Connected with PSF Deconvolution

We have demonstrated that the PSF deconvolution dramatically enhances resolution of 4D-STEM/PNBD patterns, but a question may arise if the deconvolution cannot introduce some artifacts on the final powder diffractograms. The deconvolution artifacts cannot be excluded *a priori* as the deconvolution modifies the original diffractograms, but both the experimental results (showed above in Section 3.1) and theoretical considerations (discussed below in this section) suggest that in the case of 4D-STEM/PNBD method the deconvolution artifacts were minimized to a negligible level.

As for the experimental results (Section 3.1) the strongest argument documenting that the deconvolution artifacts are insignificant after our STEMDIFF processing, is as follows: the 4D-STEM/PNBD method was applied to four independent samples (Au nanoislands, TbF₃ nanoplatelets, and two crystalline modifications of TiO₂). The four resulting diffraction profiles (Figure 2e, Figure 3e, and Figure 4a,b) contained more than 40 diffraction peaks (ca 10 observable diffractions per pattern). For *all four diffraction patterns*, the positions and intensities of the peaks in the TEM/SAED profiles (non-deconvoluted diffractograms, black lines in Figures 2–4) and 4D-STEM/PNBD profiles (deconvoluted diffractograms, red lines in Figures 2–4) were in a very good agreement. The only small exception was observed in TbF₃ diffraction profile (Figure 3e) showing a slight shift of the third diffraction peak at $q \approx 3.3 \text{ \AA}^{-1}$ to the right with respect to corresponding TEM/SAED peak (red vs. black line in Figure 3e). However, this shift could be attributed to the extremely strong preferred orientation (PO) of TbF₃ nanoplatelets, which had already been described in Section 3.2.1. In this particular case, the PO was so strong that the (theoretically) strongest diffraction (111), which was not of the preferred *hk0* type, showed a minimum in both TEM/SAED and 4D-STEM/PNBD patterns. From this point of view, the low intensity of another non-preferred diffractions (002, 221, and 131) and the resulting shift of the third peak at $q \approx 3.3 \text{ \AA}^{-1}$ towards the preferred diffraction (230) confirmed that the deconvolution further improved the results in agreement with the observed PO effect.

Yet another confirmation of the extremely strong PO in TbF₃ sample was the negligible intensity of diffraction (232) at $q \approx 4.4 \text{ \AA}^{-1}$, which should be relatively strong according to theoretical PXRD calculation (blue line in Figure 3e), but it exhibited a very weak intensity in both TEM/SAED and 4D-STEM/PNBD patterns (black, orange and red lines in Figure 3e).

Available literature and theoretical considerations support the above-discussed experimental results in the sense that deconvolution artifacts are negligible in case of 4D-STEM/PNBD method. Firstly, image deconvolution is widely used in the field of light microscopy [33–35] and the artifacts are not considered critical. Secondly, our experimentally determined PSF is based on NBD patterns with the lowest entropy, which are dominated by low spatial frequencies and contain only the broad central spot of the primary beam as documented in Figure 6. The absence of sharp edges in both PSF (a convolution mask) and individual NBD patterns (source images for convolution, whose diffraction peaks are quite broad Gaussian-like functions as evidenced in Figures 2–4, rather than sharp step functions) means that the possible *ringing artifacts* during the deconvolution are insignificant [36,37]. Thirdly, our algorithm eliminates possible artifacts due to small convolution mask, as the default STEMDIFF calculation employs a PSF function that is a few pixels larger in comparison with the original images (see parameters *psfsize* and *imgsize* in Figure 7; the detailed STEMDIFF documentation including an explanation of all parameters is available at www, as explained in Appendix A). The STEMDIFF calculation simply pushes the PSF border ring out of the area of interest.

4.4. Further Applications of 4D-STEM/PNBD Method

The specimens employed in this study were inorganic nanocrystals deposited on a thin carbon film. Analysis of nanocrystals is definitely useful by itself, but we plan to employ 4D-STEM/PNBD method also in characterization of other important types of samples: polymer nanocomposites (such as magnetic polymer microspheres filled with iron oxide nanoparticles [38]), inorganic nanoparticles in amorphous matrices (such as platinum nanoparticles in silica glass [39]), and biological samples containing nanocrystalline materials (such as calcite-precipitating bacteria [40] or biological tissues with nanocrystalline markers [41]). In these systems, a standard analysis of the inorganic nanoparticles by TEM/SAED is very difficult, as the majority of scattered electrons come from the amorphous matrix and diffractions from the nanocrystals are almost lost in the high background. The application of 4D-STEM/PNBD method should facilitate the analysis, because we could visualize the structure (using standard STEM/BF mode), select several locations with the nanocrystals, and collect signal only from the selected locations, ignoring the surrounding matrix. Preliminary results suggest that ca 10–20 nanocrystals with random orientations should be sufficient for the reliable identification of the crystalline structure by means of 4D-STEM/PNBD method.

5. Conclusions

The new version of our 4D-STEM/PNBD method converts arbitrary SEM microscope equipped with a pixelated STEM detector to a fast, high-resolution powder electron diffractometer. The 4D-STEM/PNBD method was designed for a simple, routine, and efficient everyday use with a minimal user input. It converts a huge 4D-STEM dataset, which is *easy to collect*, to a single powder diffraction pattern, which is *easy to process* even without deep crystallographic knowledge. This brings the classical *high-resolution* powder electron diffraction from the realm of TEM microscopy to the field of modern SEM microscopy and opens quite new possibilities for SEM users.

Author Contributions: Conceptualization, M.S. and R.S.; software, M.S. and R.S.; validation, M.S., R.S., E.P. and V.K.; formal analysis, M.S.; investigation, R.S., E.P. and V.K.; resources, M.S. and V.K.; data curation, M.S. and R.S.; writing—original draft preparation, M.S.; writing—review and editing, M.S., R.S. and V.K.; visualization, M.S. and R.S.; supervision, M.S.; project administration, M.S.; funding acquisition, M.S. and V.K. All authors have read and agreed to the published version of the manuscript.

Funding: This research was funded by the Technology Agency of the Czech Republic, grant number TN01000008 and Czech Science Foundation, grant number GA21-13541S.

Institutional Review Board Statement: Not applicable.

Informed Consent Statement: Not applicable.

Data Availability Statement: All data (STEM and TEM micrographs, 4D-STEM data cubes) are available at request to the first author (M.S.).

Acknowledgments: The authors thank Thermo Fisher Scientific in Brno, Czech Republic for providing the FIB-SEM Helios equipped with the T-pix detector.

Conflicts of Interest: The authors declare no conflict of interest.

Appendix A. STEMDIFF Package—Installation, Documentation, Tips and Tricks

The STEMDIFF package was designed in order to be as easy to install and employ as possible. The recent version of STEMDIFF is a standard Python package that is deposited at usual location—Python Package Index: <https://pypi.org/project/stemdiff> (accessed on 15 November 2021), from which it can be installed with a single command: `pip install stemdiff`. The package relies only on standard, well-established, and fast scientific Python modules (matplotlib, numpy, and scipy) that are included in most Python distributions [42]. The STEMDIFF user interface requires just minimal user input as explained above (Section 3.2.2). Most of the settings in the universal template (Figure 7) can be left on their default values. However, adjustments of several parameters may either improve the results or save computation time. All parameters are described in detail in the documentation available at www site of the package. The following list summarizes the most useful tips:

- **Total number of files.** The STEMDIFF calculates automatically all summations that convert 4D-STEM data to powder 2D- and 1D-diffraction patterns (i.e., summation of all files, summation of high-entropy files, and summation of high-entropy files with PSF deconvolution—as shown in Figure 5). The optimal number of files for the summation is slightly above 2000: higher numbers prolong calculation times without improving results significantly, while lower numbers may be insufficient to catch low-intensity diffractions.
- **Percentage of high-entropy files.** For summation of high-entropy files, the optimal results are usually obtained if we use 20–40% of files with the highest entropies: higher percentage prolong calculation times and diminish the filtering effect, while lower percentage may lead to less precise intensity ratios, as some less frequent crystal orientations may not be included in the filtered dataset. The exact percentage for given sample is connected with fraction of empty space between nanocrystals.
- **Number of iterations during PSF deconvolution.** For summation of high-entropy files with deconvolution, the optimal number of deconvolution iterations (using current implementation of Richardson-Lucy deconvolution algorithm in Python) usually ranges from 100–300: higher values prolong calculation times without improving the result and lower values may lead to incomplete deconvolution.
- **Smaller area of the detector employed in summations.** The edge areas of the detector may contain diffractions with very low or zero intensity. In such a case the program can be instructed to ignore edge areas of the stored files and take into consideration only central square with defined size. This may save a substantial amount of computing time needed for PSF deconvolution step.

- **Upsampling.** Contemporary pixelated STEM detectors have limited resolution. The modern DED detector employed in this work was an array of 256×256 pixels. The STEMDIFF program increases (i.e., upsamples) the resolution 4 times to 1024×1024 pixels, which is comparable to TEM cameras. The additional points are interpolated (using 2D bicubic interpolation algorithm). The upsampling constant can be adjusted by the user, but the resolution 1024×1024 was found optimal: a lower resolution led to rough profiles and a higher resolution increased the computation times considerably without any significant benefit. In this contribution, all 2D- and 1D-diffraction patterns are shown after the fourfold upsampling.

Appendix B. STEMDIFF Package—MATLAB Version

The STEMDIFF package was programmed not only in Python (as described above in Section 3.2), but also in MATLAB. Both versions are free and equivalent in the sense that they yield almost identical results. Users can choose either of them, depending if they prefer Python (freeware) or MATLAB environment (commercial). The MATLAB version is based on very intuitive *Live Editor* interface, which combines text descriptions, code and computed results. It can be downloaded from Mathworks®File Exchange site (<https://www.mathworks.com/matlabcentral/fileexchange> (accessed on 15 November 2021) → Search → stemdiff). The user interface of the MATLAB version is shown in Figure A1.

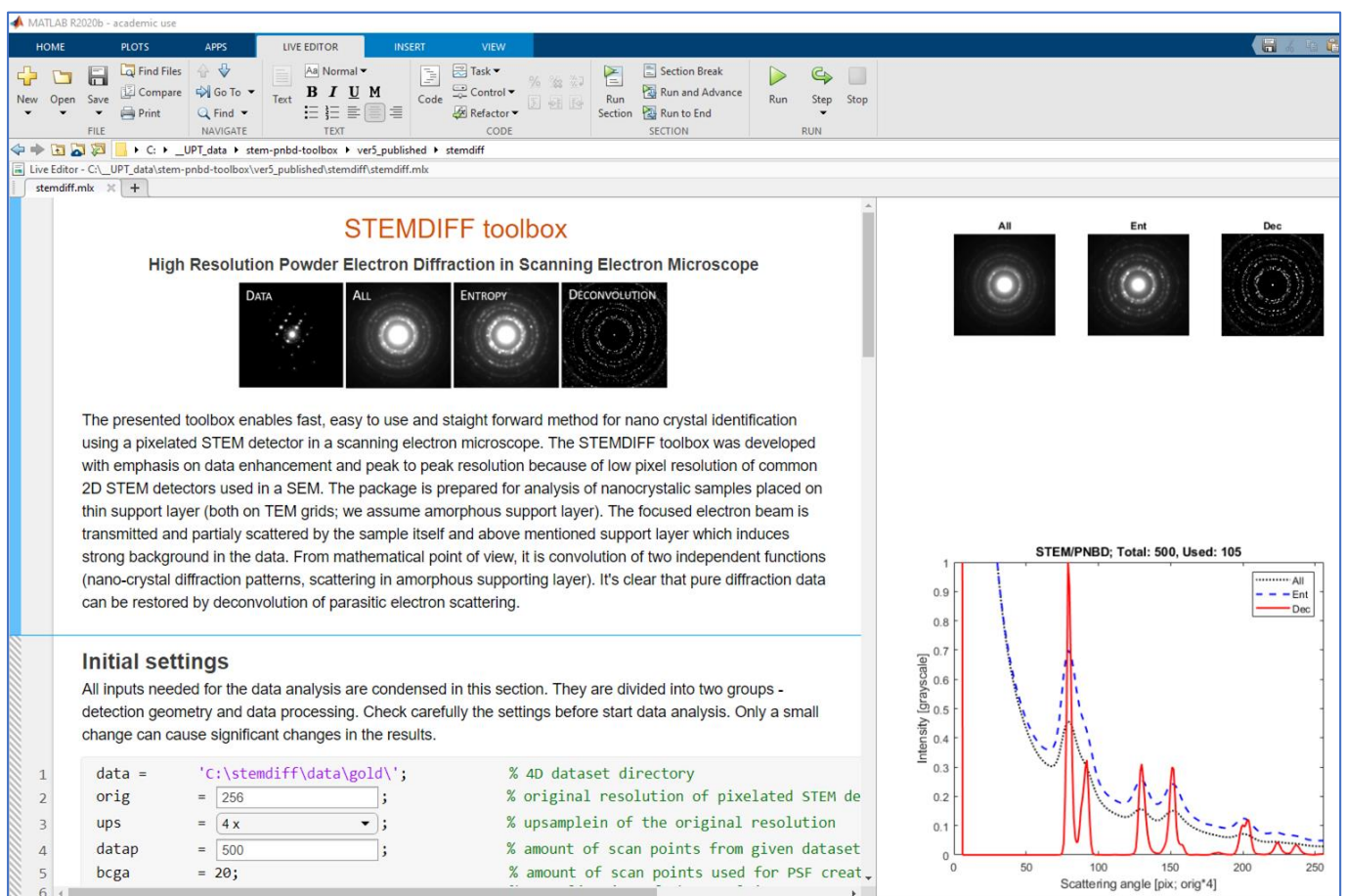


Figure A1. The MATLAB interface of the STEMDIFF toolbox shows the code, comments and results in one place.

From the user's point of view, the Python and MATLAB versions of STEMDIFF package are quite similar. As for MATLAB, the user just downloads STEMDIFF toolbox, opens *stemdiff.mlx* file (shipped within the toolbox), modifies a few input parameters and runs the script. All input parameters are placed and described together in *Initial settings*

section as illustrated in Figure A1. After running *stemdiff.mlx*, the outputs are shown in the right results window (Figure A1, right pane) and saved automatically in TXT- and JPG-formatted files in the working directory if option “save to file” is switched to “YES”. Additional information and help can be found directly in the textual descriptions within the STEMDIFF toolbox.

Appendix C. Reliability and Reproducibility of 4D-STEM/PNBD Method

The reliability and reproducibility of our 4D-STEM/PNBD method was verified by comparison of results from two different datasets, which were measured at different locations of the same sample. This test was performed for Au nanoislands (Figure A2a) and TbF₃ nanocrystals (Figure A2b). For each sample, we compared the original 4D-STEM dataset, which was used in the main text of this work (dataset #1 in Figure A2a,b) and an additionally measured dataset of the same size, which was measured at different location using the same experimental conditions (dataset #2 in Figure A2a,b). The datasets #1 and #2 were processed by STEMDIFF using the same calculation parameters and the results were almost identical (compare orange lines and black dotted lines in Figure A2a,b). Therefore, we can conclude that our 4D-STEM/PNBD method yields reliable and reproducible results.

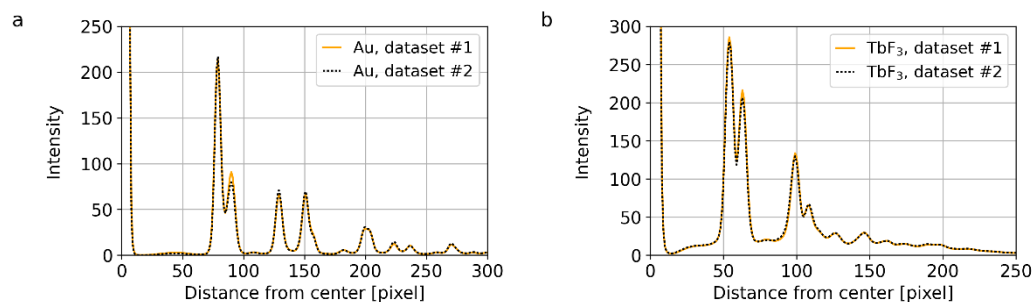


Figure A2. Final 4D-STEM/PNBD profiles (after entropy filtering and PSF-deconvolution) calculated for two independent datasets with the same experimental and processing parameters: (a) Au-nanoislands and (b) TbF₃ nanocrystals.

References

1. Watt, I.M. *The Principles and Practice of Electron Microscopy*, 2nd ed.; Cambridge University Press: Cambridge, UK, 1997; p. 500.
2. Shibata, N.; Kohno, Y.; Findlay, S.D.; Sawada, H.; Kondo, Y.; Ikuhara, Y. New area detector for atomic-resolution scanning transmission electron microscopy. *J. Electron. Microsc. (Tokyo)* **2010**, *59*, 473–479. [[CrossRef](#)] [[PubMed](#)]
3. Skoupy, R.; Nebesarova, J.; Slouf, M.; Krzyzaneck, V. Quantitative STEM imaging of electron beam induced mass loss of epoxy resin sections. *Ultramicroscopy* **2019**, *202*, 44–50. [[CrossRef](#)]
4. Sun, C.; Muller, E.; Meffert, M.; Gerthsen, D. On the Progress of Scanning Transmission Electron Microscopy (STEM) Imaging in a Scanning Electron Microscope. *Microsc. Microanal.* **2018**, *24*, 99–106. [[CrossRef](#)] [[PubMed](#)]
5. Beche, A.; Rouviere, J.L.; Barnes, J.P.; Cooper, D. Strain measurement at the nanoscale: Comparison between convergent beam electron diffraction, nano-beam electron diffraction, high resolution imaging and dark field electron holography. *Ultramicroscopy* **2013**, *131*, 10–23. [[CrossRef](#)]
6. Faruqi, A.R.; McMullan, G. Direct imaging detectors for electron microscopy. *Nucl. Instrum. Methods Phys. Res. Sect. A* **2018**, *878*, 180–190. [[CrossRef](#)]
7. MacLaren, I.; Macgregor, T.A.; Allen, C.S.; Kirkland, A.I. Detectors—The ongoing revolution in scanning transmission electron microscopy and why this important to material characterization. *APL Mater.* **2020**, *8*, 110901. [[CrossRef](#)]
8. Ophus, C. Four-Dimensional Scanning Transmission Electron Microscopy (4D-STEM): From Scanning Nanodiffraction to Ptychography and Beyond. *Microsc. Microanal.* **2019**, *25*, 563–582. [[CrossRef](#)]
9. Savitzky, B.H.; Zeltmann, S.E.; Hughes, L.A.; Brown, H.G.; Zhao, S.; Pelz, P.M.; Pekin, T.C.; Barnard, E.S.; Donohue, J.; Rangel DaCosta, L.; et al. py4DSTEM: A Software Package for Four-Dimensional Scanning Transmission Electron Microscopy Data Analysis. *Microsc. Microanal.* **2021**, *27*, 712–743. [[CrossRef](#)]
10. Vystavěl, T.; Tůma, L.; Stejskal, P.; Unčovský, M.; Skalický, J.; Young, R. Expanding Capabilities of Low-kV STEM Imaging and Transmission Electron Diffraction in FIB/SEM Systems. *Microsc. Microanal.* **2017**, *23*, 554–555. [[CrossRef](#)]
11. Holm, J.D.; Caplins, B.W. *STEM in SEM: Introduction to Scanning Transmission Electron Microscopy for Microelectronics Failure Analysis*; ASM International: Novelty, OH, USA, 2020.

12. Caplins, B.W.; Holm, J.D.; Keller, R.R. Orientation mapping of graphene in a scanning electron microscope. *Carbon* **2019**, *149*, 400–406. [[CrossRef](#)]
13. Caplins, B.W.; Holm, J.D.; White, R.M.; Keller, R.R. Orientation mapping of graphene using 4D STEM-in-SEM. *Ultramicroscopy* **2020**, *219*, 113137. [[CrossRef](#)]
14. Schweizer, P.; Denninger, P.; Dolle, C.; Spiecker, E. Low energy nano diffraction (LEND)—A versatile diffraction technique in SEM. *Ultramicroscopy* **2020**, *213*, 112956. [[CrossRef](#)] [[PubMed](#)]
15. Slouf, M.; Skoupy, R.; Pavlova, E.; Krzyzanek, V. Powder Nano-Beam Diffraction in Scanning Electron Microscope: Fast and Simple Method for Analysis of Nanoparticle Crystal Structure. *Nanomaterials* **2021**, *11*, 962. [[CrossRef](#)] [[PubMed](#)]
16. Labar, J.L.; Adamik, M.; Barna, B.P.; Czigany, Z.; Fogarassy, Z.; Horvath, Z.E.; Geszti, O.; Misjak, F.; Morgiel, J.; Radnoczi, G.; et al. Electron diffraction based analysis of phase fractions and texture in nanocrystalline thin films, Part III: Application examples. *Microsc. Microanal.* **2012**, *18*, 406–420. [[CrossRef](#)] [[PubMed](#)]
17. Slouf, M.; Vacková, T.; Zhigunov, A.; Sikora, A.; Piorkowska, E. Nucleation of Polypropylene Crystallization with Gold Nanoparticles. Part 2: Relation between Particle Morphology and Nucleation Activity. *J. Macromol. Sci. Part B* **2016**, *55*, 393–410. [[CrossRef](#)]
18. Shapoval, O.; Oleksa, V.; Slouf, M.; Lobaz, V.; Trhlikova, O.; Filipova, M.; Janouskova, O.; Engstova, H.; Pankrac, J.; Modry, A.; et al. Colloidally Stable P(DMA-AGME)-Ale-Coated Gd(Tb)F₃:Tb(3+)(Gd(3+)),Yb(3+),Nd(3+) Nanoparticles as a Multimodal Contrast Agent for Down- and Upconversion Luminescence, Magnetic Resonance Imaging, and Computed Tomography. *Nanomaterials* **2021**, *11*, 230. [[CrossRef](#)]
19. Kraus, W.; Nolze, G. POWDER CELL—A program for the representation and manipulation of crystal structures and calculation of the resulting X-ray powder patterns. *J. Appl. Crystallogr.* **1996**, *29*, 301–303. [[CrossRef](#)]
20. Glasser, L. Crystallographic Information Resources. *J. Chem. Educ.* **2016**, *93*, 542–549. [[CrossRef](#)]
21. Granja, C.; Jakubek, J.; Polansky, S.; Zach, V.; Krist, P.; Chvatil, D.; Stursa, J.; Sommer, M.; Ploc, O.; Kodaira, S.; et al. Resolving power of pixel detector Timepix for wide-range electron, proton and ion detection. *Nucl. Instrum. Methods Phys. Res. Sect. A* **2018**, *908*, 60–71. [[CrossRef](#)]
22. Andrews, K.W.; Dyson, D.J.; Keown, S.R. *Interpretation of Electron Diffraction Patterns*; Plenum Press: New York, NY, USA, 1967.
23. Shannon, C.E. A Mathematical Theory of Communication. *Bell Syst. Tech. J.* **1948**, *27*, 379–423. [[CrossRef](#)]
24. Fabbri, R.; Gonçalves, W.N.; Lopes, F.J.P.; Bruno, O.M. Multi-q pattern analysis: A case study in image classification. *Phys. A Stat. Mech. Appl.* **2012**, *391*, 4487–4496. [[CrossRef](#)]
25. Nord, M.; Webster, R.W.H.; Paton, K.A.; McVitie, S.; McGrouther, D.; MacLaren, I.; Paterson, G.W. Fast Pixelated Detectors in Scanning Transmission Electron Microscopy. Part I: Data Acquisition, Live Processing, and Storage. *Microsc. Microanal.* **2020**, *26*, 653–666. [[CrossRef](#)] [[PubMed](#)]
26. Moskvin, M.; Huntosova, V.; Herynek, V.; Matous, P.; Michalcova, A.; Lobaz, V.; Zasonska, B.; Slouf, M.; Seliga, R.; Horak, D. In vitro cellular activity of maghemite/cerium oxide magnetic nanoparticles with antioxidant properties. *Colloids Surf. B Biointerfaces* **2021**, *204*, 111824. [[CrossRef](#)]
27. Momma, K.; Izumi, F. VESTA 3 for three-dimensional visualization of crystal, volumetric and morphology data. *J. Appl. Crystallogr.* **2011**, *44*, 1272–1276. [[CrossRef](#)]
28. Gammer, C.; Burak Ozdol, V.; Liebscher, C.H.; Minor, A.M. Diffraction contrast imaging using virtual apertures. *Ultramicroscopy* **2015**, *155*, 1–10. [[CrossRef](#)]
29. Shukla, A.K.; Ramasse, Q.M.; Ophus, C.; Kepaptsoglou, D.M.; Hage, F.S.; Gammer, C.; Bowling, C.; Gallegos, P.A.H.; Venkatachalam, S. Effect of composition on the structure of lithium- and manganese-rich transition metal oxides. *Energy Environ. Sci.* **2018**, *11*, 830–840. [[CrossRef](#)]
30. Allen, F.I.; Pekin, T.C.; Persaud, A.; Rozeveld, S.J.; Meyers, G.F.; Ciston, J.; Ophus, C.; Minor, A.M. Fast Grain Mapping with Sub-Nanometer Resolution Using 4D-STEM with Grain Classification by Principal Component Analysis and Non-Negative Matrix Factorization. *Microsc. Microanal.* **2021**, *27*, 794–803. [[CrossRef](#)]
31. Pekin, T.C.; Gammer, C.; Ciston, J.; Ophus, C.; Minor, A.M. In situ nanobeam electron diffraction strain mapping of planar slip in stainless steel. *Scr. Mater.* **2018**, *146*, 87–90. [[CrossRef](#)]
32. Jiang, Y.; Chen, Z.; Han, Y.; Deb, P.; Gao, H.; Xie, S.; Purohit, P.; Tate, M.W.; Park, J.; Gruner, S.M.; et al. Electron ptychography of 2D materials to deep sub-angstrom resolution. *Nature* **2018**, *559*, 343–349. [[CrossRef](#)]
33. Guo, M.; Li, Y.; Su, Y.; Lambert, T.; Nogare, D.D.; Moyle, M.W.; Duncan, L.H.; Ikegami, R.; Santella, A.; Rey-Suarez, I.; et al. Rapid image deconvolution and multiview fusion for optical microscopy. *Nat. Biotechnol.* **2020**, *38*, 1337–1346. [[CrossRef](#)]
34. Sage, D.; Donati, L.; Soulez, F.; Fortun, D.; Schmit, G.; Seitz, A.; Guiet, R.; Vonesch, C.; Unser, M. DeconvolutionLab2: An open-source software for deconvolution microscopy. *Methods* **2017**, *115*, 28–41. [[CrossRef](#)] [[PubMed](#)]
35. Sarder, P.; Nehorai, A. Deconvolution methods for 3-D fluorescence microscopy images. *IEEE Signal Process. Mag.* **2006**, *23*, 32–45. [[CrossRef](#)]
36. McBride, W.; Cockayne, D.J.H.; Tsuda, K. Deconvolution of electron diffraction patterns of amorphous materials formed with convergent beam. *Ultramicroscopy* **2003**, *94*, 305–308. [[CrossRef](#)]
37. Zuo, B.; Hu, X.; Cai, Z.; Tian, J. Deconvolution image ringing artifacts removal via anisotropic diffusion. *Opt. Eng.* **2012**, *51*, 057001. [[CrossRef](#)]

38. Horák, D.; Hlídková, H.; Trachtová, Š.; Šlouf, M.; Rittich, B.; Španová, A. Evaluation of poly(ethylene glycol)-coated monodispersed magnetic poly(2-hydroxyethyl methacrylate) and poly(glycidyl methacrylate) microspheres by PCR. *Eur. Polym. J.* **2015**, *68*, 687–696. [[CrossRef](#)]
39. Tarkistani, M.A.M.; Komalla, V.; Kayser, V. Recent Advances in the Use of Iron-Gold Hybrid Nanoparticles for Biomedical Applications. *Nanomaterials* **2021**, *11*, 1227. [[CrossRef](#)]
40. Mansor, M.; Hamilton, T.L.; Fantle, M.S.; Macalady, J.L. Metabolic diversity and ecological niches of *Achromatium* populations revealed with single-cell genomic sequencing. *Front. Microbiol.* **2015**, *6*, 822. [[CrossRef](#)] [[PubMed](#)]
41. Torres-Torres, D.; Bornacelli, J.; Vega-Becerra, O.; Garay-Tapia, A.M.; Aguirre-Tostado, F.S.; Torres-Torres, C.; Oliver, A. Magnetic Force Microscopy Study of Multiscale Ion-Implanted Platinum in Silica Glass, Recorded by an Ultrafast Two-Wave Mixing Configuration. *Microsc. Microanal.* **2020**, *26*, 53–62. [[CrossRef](#)] [[PubMed](#)]
42. VanderPlas, J. *Python Data Science Handbook*; O'Reilly Media, Inc.: Sebastopol, CA, USA, 2017; p. 529.